Sustainable Energy & Fuels

ROYAL SOCIETY OF CHEMISTRY

PAPER

View Article Online
View Journal | View Issue

Cite this: *Sustainable Energy Fuels*, 2019, **3**, 2409

Confined growth of $MoSe_2$ nanosheets in N-doped carbon shell with hierarchical porous structure for efficient hydrogen evolution†

Zhiqian Cao, [a] Haibo Hu, *[a] Mingzai Wu, *[a] Chuanjun Tu, *[b]
Dawei Zhang [c] and Zongquan Wu [c]

Received 21st May 2019
Accepted 4th July 2019

DOI: 10.1039/c9se00311h

rsc.li/sustainable-energy

Construction of reasonable composite architecture to enhance the robustness, alleviate the aggregation, and simultaneously improve the intrinsic poor conductivity is the key to realizing the synthesis of highly efficient noble-metal-free $MoSe_2$-based electrocatalysts for the hydrogen evolution reaction (HER). Herein, space-confined $MoSe_2$ nanosheets grown in an N-doped carbon shell with a hierarchical porous structure (defined as $MoSe_2$/NDC) were designed and fabricated, which acquire improved conductivity and more exposed active sites for hydrogen atom adsorption, exhibiting excellent HER activity both in alkaline and acidic media with a small overpotential of 155/142 mV at a current density of 10 mA cm^{-2}, and a Tafel slope of 68/62 mV dec^{-1}, respectively. More importantly, thanks to the protection of the outermost N-doped carbon layer, the $MoSe_2$/NDC shows excellent durability, with almost no attenuation observed in the time-dependent current density curve at an applied constant overpotential of 155/142 mV up to 24 hours in alkaline or acidic media. The following density functional theory (DFT) calculation results reveal that the excellent HER activity of $MoSe_2$/NDC composites originates from the substantially reduced $|\Delta G_{H*}|$ of the intermediate adsorbed hydrogen. The strategy of *in situ* space-confined-growth combined with the design of a composite hierarchical porous structure provides an efficient solution to fabricate high-performance $MoSe_2$-based pH-universal electrocatalysts for hydrogen production.

Introduction

With the rapid consumption of unsustainable ore energy and the subsequently increasing severe environmental pollution, the exploitation of clean and sustainable alternative energy resources is becoming increasingly urgent.[1–3] Hydrogen is considered to be an ideal alternative energy to fossil fuels by virtue of its zero carbon emissions and high combustion value.[4,5] It is universally acknowledged that electrocatalytic water splitting *via* the hydrogen evolution reaction (HER) is an effective, secure, and sustainable means for large-scale hydrogen production.[6,7] In order to realize efficient water splitting, design and preparation of high-performance electrocatalysts for promoting the HER is key.[8–10] To date, depending on excellent catalytic activity and corrosion resistance, Pt-based metal catalysts are identified to be the most efficient electrocatalysts for the HER, but scarcity and high cost cast a shadow on their wide commercial applications in the future.[11,12] In this context, development of low-cost, resource-rich and environmentally friendly noble-metal-free HER electrocatalysts with high catalytic activity and durability is still highly desired but a great challenge.

Recently, many efforts have been devoted to exploring non-precious-metal catalysts,[13–16] such as Mo_2C,[17–21] MoP,[22–24] MoS_2,[25–27] $MoSe_2$,[28–30] and other molybdenum-based catalysts.[31–33] Delightingly, these studies suggest that these molybdenum-based catalysts are a kind of class promising alternative electrocatalysts to Pt in a variety of reactions including the HER, owing to their abundance, low cost, and high activity. Among them, by virtue of near-zero Gibbs free energy for hydrogen adsorption on abundant exposed active edges, $MoSe_2$ nanosheets with a unique layered structure have shown greater potential for use as an efficient non-precious-metal electrocatalyst for the HER.[34–36] Nevertheless, their potential electrocatalytic activity in the HER is severely inhibited by incomplete exposure of active sites mainly caused by their close restacking and intrinsic poor conductivity,[37,38] which makes achieving a good theoretical performance difficult. In addition, most of

---

[a] *School of Physics and Materials Science, Anhui University, Hefei, China. E-mail: haibohu@ahu.edu.cn; wumz@ahu.edu.cn*

[b] *School of Materials Science and Engineering, Hunan University, Changsha, China. E-mail: tcj@hnu.edu.cn*

[c] *Anhui Province Key Laboratory of Advanced Catalytic Materials and Reaction Engineering, Hefei University of Technology, Hefei, China*

† Electronic supplementary information (ESI) available: Experimental section; calculation details; typical SEM images of the NDC and the $MoSe_2$; thermogravimetric (TGA) curves of the NDC and $MoSe_2$/NDC at a heating rate of 10 °C min^{-1} in a flowing air environment; SEM images of the $MoSe_2$/NDC electrocatalyst after 10 000 cycles in 1 M KOH and 0.5 M H_2SO_4. See DOI: 10.1039/c9se00311h

the transition metal chalcogenides are easily corroded in strong corrosive electrolyte, especially in acidic media, thus greatly reducing the stability of the catalysts and the catalytic efficiency. Compared to strongly corrosive acidic electrolyte, alkaline electrolyte has a less corrosive effect on transition metal chalcogenides. Thus, alkaline electrolyte is a more desirable medium for large-scale production of hydrogen *via* the HER, which is conducive to sustainable application of transition metal chalcogenide based electrocatalysts for water splitting, guaranteeing cost-effectiveness.[39] Consequently, construction of a rational composite structure to alleviate the aggregation, simultaneously improve the intrinsic poor conductivity of $MoSe_2$ nanosheets, and more importantly, enhance their durability in alkaline media is essential to exploit the potential performance of $MoSe_2$-based electrocatalysts in the HER.

Carbonaceous materials,[8,40] especially nitrogen or sulfur doped carbon materials, by virtue of their excellent conductivity and corrosion resistance, as well as certain catalytic activity, have been used as ideal carriers for supporting transition metal chalcogenide based nanocatalysts to improve their poor electrical conductivity and inhibit aggregation during operation, realizing improvement of catalytic activity in acidic media.[13,41] However, these studies still face some challenges such as a cumbersome and complex preparation process, low production efficiency, and more importantly, relatively low HER activity in more desirable alkaline media.

Herein, aiming at addressing the above-mentioned challenges and exploiting the potential catalytic activity of $MoSe_2$-based electrocatalysts for the HER in more desirable alkaline media, space-confined $MoSe_2$ nanosheets grown in a dopamine-derived N-doped carbon shell with a hierarchical porous structure (defined as $MoSe_2$/NDC) were designed and fabricated through a simple strategy. The employed space-confined strategy realizes the growth of $MoSe_2$ nanosheets in an N-doped carbon shell, which effectively alleviates the restacking of $MoSe_2$ nanosheets, allowing more exposed active sites for hydrogen atom adsorption. Meanwhile, the encapsulation of $MoSe_2$ nanosheets with an N-doped carbon shell improves the intrinsic poor conductivity of $MoSe_2$ nanosheets, promoting the electron transport and charge transfer at the interface. More importantly, the outer N-doped carbon shell, serving as a protection layer, can effectively prevent $MoSe_2$ nanosheets from corrosion, resulting in enhanced durability in corrosive electrolyte. Finally, the synchronous construction of a 3D hierarchical porous structure facilitates the adsorption of electrolyte, boosting exposure of more active sites for hydrogen atom adsorption. As expected, the as-fabricated $MoSe_2$/NDC composite electrocatalysts exhibit excellent HER activity and durability both in alkaline and acidic media with a small overpotential of 155 mV/142 mV at a current density of 10 mA cm^{-2}, and a Tafel slope of 68 mV dec^{-1}/62 mV dec^{-1}, respectively. Density functional theory (DFT) simulations were further carried out to study the adsorption and desorption behavior of the intermediate adsorbed hydrogen, indicating that the substantially reduced $|\Delta G_{H*}|$ of the intermediate adsorbed hydrogen should be responsible for the excellent HER activity of $MoSe_2$/NDC composites. All these results make the strategy of *in situ* space-confined growth combined with the design of a hierarchical porous structure an efficient solution to fabricate high-efficient $MoSe_2$-based pH-universal electrocatalysts for hydrogen production.

Results and discussion

Preparation and characterization of $MoSe_2$/NDC composite electrocatalysts

The detailed preparation procedure of the $MoSe_2$/NDC composite electrocatalysts is schematically illustrated in Fig. 1a. The easily manipulated synthesis protocol first began with mixing ammonia water, dopamine hydrochloride, ammonium molybdate and ethanol solution to prepare the Mo-precursor mixture, during which the Mo element was confined in self-polymerized polydopamine *via* a chelation reaction between abundant ammonium pairs and Mo ions. Then, the Mo-precursor mixture underwent a freeze-drying process to form a loose porous structure, in order to facilitate the subsequent selenization process in a chemical vapor deposition (CVD) tube furnace. During the process, polydopamine was pyrolyzed into an N-doped carbon (NDC) shell encapsulating the synchronously space-confined monodisperse $MoSe_2$ nanosheets, resulting in the synthesis of $MoSe_2$/NDC composites with a hierarchical porous structure. The detailed synthesis process is shown in the Experimental section in the ESI.†

The morphology and microstructure of the as-fabricated $MoSe_2$/NDC composites, pure $MoSe_2$ and NDC contrastive samples were first characterized with Scanning Electron Microscopy (SEM), Transmission Electron Microscopy (TEM) and High Resolution Transmission Electron Microscopy (HRTEM). From an overall view (Fig. 1b), the $MoSe_2$/NDC sample consists of uniform flower-like porous microspheres with average size distribution. The close-up view further clearly shows that the individual microsphere has a hierarchical porous structure assembled from numerous ultrathin $MoSe_2$ nanosheets encapsulated by an N-doped carbon shell (Fig. 1c). The Brunauer–Emmett–Teller (BET) surface area and porosity of the $MoSe_2$/NDC were further analyzed using N_2 adsorption–desorption isotherms. Fig. 1d displays a type-IV isotherm with a distinct hysteresis loop, indicating the presence of lots of micro/mesopores in $MoSe_2$/NDC composites. Such a hierarchically micro/mesoporous structure was also reflected by the pore size distributions (Fig. 1d, inset). The lager BET surface area (220 m^2 g^{-1}) of the $MoSe_2$/NDC is of great significance for catalytic application, which can effectively facilitate exposure of active sites and rapid transport of HER-related species. Fig. 1e shows EDS-mapping of $MoSe_2$/NDC composites, revealing the presence and uniform distribution of C, N, Se, and Mo elements in the $MoSe_2$/NDC sample. The corresponding TEM images of $MoSe_2$/NDC samples further confirm that the $MoSe_2$ ultrathin nanosheets encapsulated in an N-doped carbon shell self-assembled together to form flower-like microspheres with a hierarchical porous structure (Fig. 1f–h). The inset of Fig. 1h shows the HRTEM image of $MoSe_2$/NDC, in which the measured interplanar spacing of 0.65 nm is attributed to the (002) planes of $MoSe_2$, also demonstrating the generation of

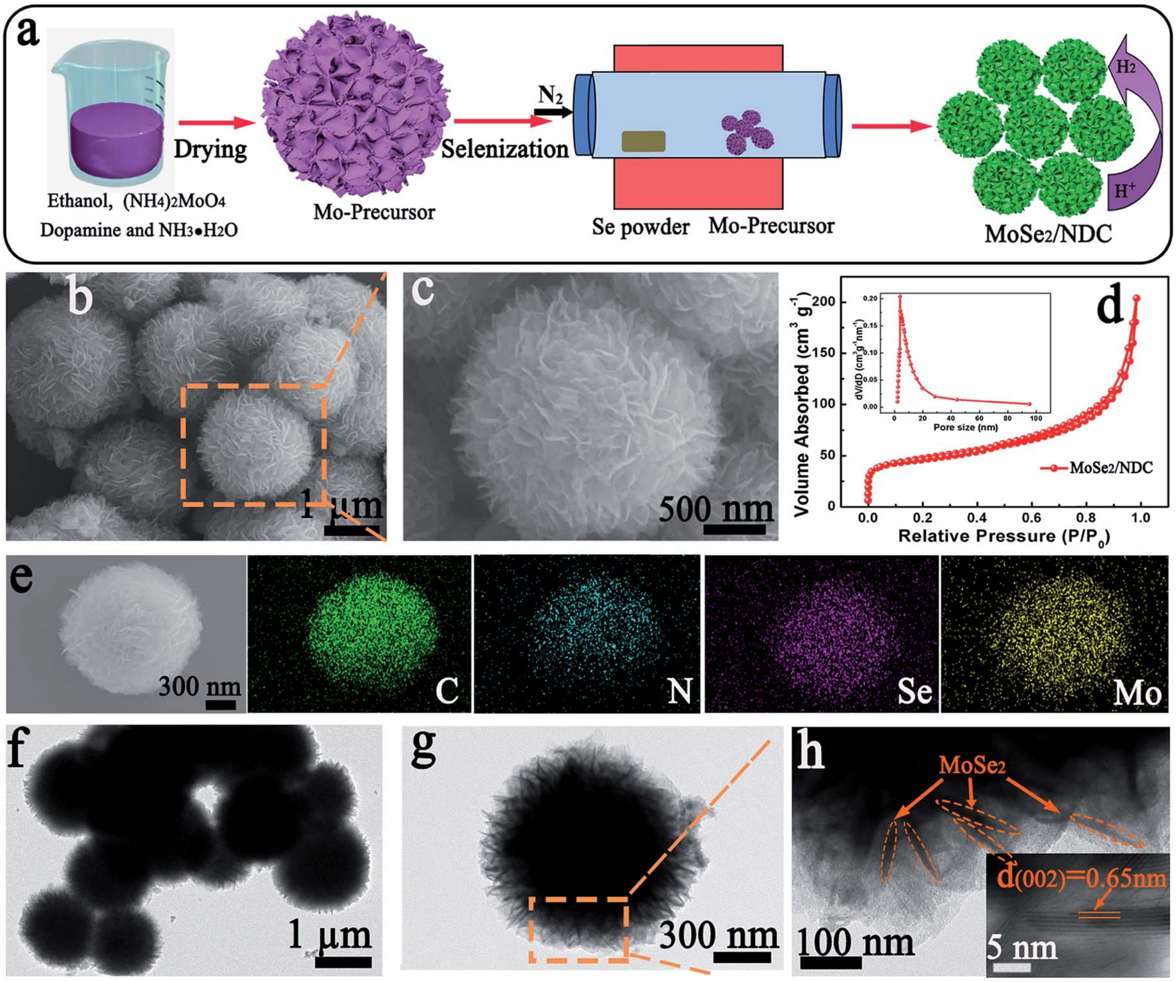

Fig. 1 (a) Flowchart of the easily manipulated synthesis protocol for the $MoSe_2$/NDC composite electrocatalysts. Typical SEM images of (b and c) the as-obtained $MoSe_2$/NDC composites; (d) N_2 adsorption–desorption isotherms (inset: BJH pore-size); (e) the SEM image and corresponding C, N, Se, and Mo elemental mapping of the prepared $MoSe_2$/NDC composites; (f–h) typical TEM images of the $MoSe_2$/NDC composites; inset in (h): the corresponding HRTEM image of the $MoSe_2$/NDC composites.

$MoSe_2$ sheets in the $MoSe_2$/NDC composites. For comparison, pure $MoSe_2$ and NDC samples were also prepared without dopamine and ammonium molybdate using the same procedure, respectively. As clearly shown in Fig. S1,† the as-obtained pure $MoSe_2$ samples present a rough sheet structure without a hierarchical porous structure and the NDC is mainly in the form of smooth 0-dimensional microspheres. In contrast, the $MoSe_2$/NDC composites have a flower-like hierarchical porous structure, formed during our preparation strategy.

X-ray diffraction (XRD) was further used to determine the crystalline phase of the synthesized samples. As shown in Fig. 2a, the $MoSe_2$/NDC samples display obvious diffraction peaks at $2\theta = 13.2°$, $27.5°$, $31.9°$, $38.1°$, $47.1°$, $56.2°$, $65.7°$, $70.2°$ and $72.8°$, corresponding to the (002), (004), (100), (103), (105), (110), (200), (203), and (116) planes of hexagonal $MoSe_2$ (JCPDS 87-2419),[42–44] respectively, directly demonstrating the existence of $MoSe_2$ nanocrystals in the product. A broad peak ranging from $2\theta = 20°$ to $30°$ observed in the XRD pattern of NDC is ascribed to carbonaceous matrices. In contrast, there is not a similar carbon peak observed in the XRD pattern of $MoSe_2$/NDC. We think this phenomenon is mainly due to the high intensity of the diffraction peaks attributed to the $MoSe_2$ nanocrystals, covering up the relatively weak diffraction peak attributed to the carbon. In order to confirm the coexistence of $MoSe_2$ and NDC in the composite materials, a representative Raman spectrum of the as-obtained $MoSe_2$/NDC composites is further shown in Fig. 2b, which can be divided into two parts: <500 cm^{-1} and >500 cm^{-1}. The Raman bands below 500 cm^{-1} can be indexed to $MoSe_2$, and those above 500 cm^{-1} are related to amorphous carbon in the $MoSe_2$/NDC sample. As shown in Fig. 2b, typical D and G bands of amorphous carbon located at 1369 and 1583 cm^{-1} were obviously observed in the spectrum, directly indicating the formation of carbonaceous composites after pyrolysis. The relative intensity ratio of the D band to the G band (I_D/I_G) has been widely adopted for evaluating the defect degree of carbon.[45–47] The I_D/I_G ratio of $MoSe_2$/NDC (0.95) is slightly lower than that of the NDC (0.96), which can be attributed to the N heteroatom doping. The N heteroatom doping would induce many defects in the internal portion of the

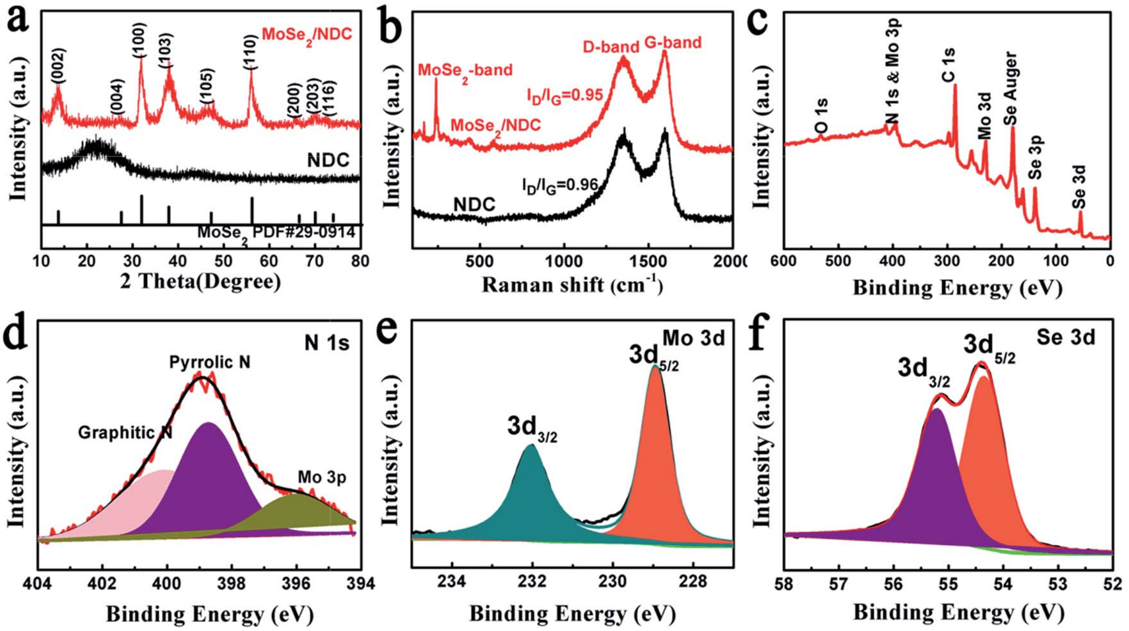

Fig. 2 (a) XRD patterns of the NDC and $MoSe_2$/NDC; (b) Raman spectra of NDC and $MoSe_2$/NDC; XPS spectra of $MoSe_2$/NDC: (c) survey spectrum, (d) N 1s, (e) Mo 3d, and (f) Se 3d.

hierarchical porous carbon skeleton, resulting in improved catalytic activity of the composite electrocatalysts.

X-ray photoelectron spectra (XPS) measurements were further carried out to analyze the chemical composition and state of the $MoSe_2$/NDC *in situ* composites. The wide-scan XPS spectrum shown in Fig. 2c reveals clear XPS peaks attributed to C, N, Mo, and Se, demonstrating no other detectable impurities for $MoSe_2$. For the high resolution N 1s XPS spectrum (Fig. 2d), the N 1s peak can also be deconvoluted into two peaks, corresponding to pyrrolic N (398.6 eV) and graphitic N (400.4 eV), indicating successful N doping in the carbon matrix.[4,13,26] As for the Mo 3d XPS spectrum shown in Fig. 2e, the displayed peaks at approximately 228.5 and 231.6 eV can be attributed to the Mo $3d_{5/2}$ and Mo $3d_{3/2}$ energies of $MoSe_2$, respectively.[39,48] The Se 3d spectrum in Fig. 2f shows peaks at approximately 54.0 and 54.9 eV, which are assigned to the Se $3d_{5/2}$ and Se $3d_{3/2}$ binding energies of $MoSe_2$, respectively.[34,38,49] Moreover, the estimated atomic weight percentages are 79.19% for C, 2.47% for N, 6.02% for Mo, and 12.32% for Se, respectively, which reveals that the atomic ratio of Mo : Se is approximately 1 : 2.05, consistent with the atomic ratio of Mo : Se in the chemical molecular formula of $MoSe_2$. The typical thermal gravimetric analysis (TGA) curve (Fig. S2†) further reveals the weight loss of the as-prepared NDC and $MoSe_2$/NDC samples with the temperature increase from 30–900 °C in air. It can be seen that the sample has an initial loss of weight about 10.2 wt% below 400 °C, which can be ascribed to the removal of absorbed water and air. In addition, there is a significant weight drop at the temperature range from 400 to 500 °C, which is due to the weight loss of carbon elements. Finally, the remnant product (21.6 wt%) is mainly MoO_3 transformed from $MoSe_2$ during the thermogravimetric process in the air. Thus, according to the law of conservation of elements (the content of Mo in MoO_3 is equal to that in $MoSe_2$), the percentage of $MoSe_2$ in the $MoSe_2$/NDC composite is calculated to be 38.1 wt%. All of the above results clearly indicate the successful preparation of $MoSe_2$/NDC composites.

Electrocatalytic activity of $MoSe_2$/NDC composites in alkaline and acidic media

The electrocatalytic HER activities of the as-fabricated $MoSe_2$/NDC composite electrocatalyst in alkaline media were first investigated using a standard three-electrode system in N_2-saturated 1.0 M KOH electrolyte and compared to those of the pure NDC, $MoSe_2$, and commercial 20% Pt/C contrastive samples. As shown in Fig. 3a and b, thanks to the reasonable structure design, the as-fabricated $MoSe_2$/NDC composite electrocatalyst exhibits a low onset potential of 83 mV (*vs.* RHE) and an overpotential of 155 mV (*vs.* RHE) at a cathodic current density of 10 mA cm^{-2}. In contrast, the overpotential of the pure NDC and $MoSe_2$ is 871 and 518 mV (*vs.* RHE) at a current density of 10 mA cm^{-2} (η_{10}), respectively. The lower overpotential represents the higher HER activity of the $MoSe_2$/NDC composite electrocatalyst than that of NDC and $MoSe_2$. The corresponding Tafel slope values for the NGC, $MoSe_2$, $MoSe_2$/NDC, and commercial 20% Pt/C were further calculated to be 321, 182, 68, and 38 mV dec^{-1}, respectively, as shown in Fig. 3c, which can be deduced from the Tafel equation ($\eta = b \log j + a$, where η is the overpotential, j is the current density and b is the Tafel slope).[30] Generally, the smaller Tafel slope means faster kinetics of hydrogen generation efficiency. Thus, apparently, $MoSe_2$/NDC *in situ* composites possess a lower Tafel slope of 68 mV dec^{-1} than those of NDC (321 mV dec^{-1}) and $MoSe_2$ (182 mV dec^{-1}), close to the value of the commercial 20% Pt/C catalyst (38 mV dec^{-1}), indicating the superior HER activity of $MoSe_2$/NDC. The

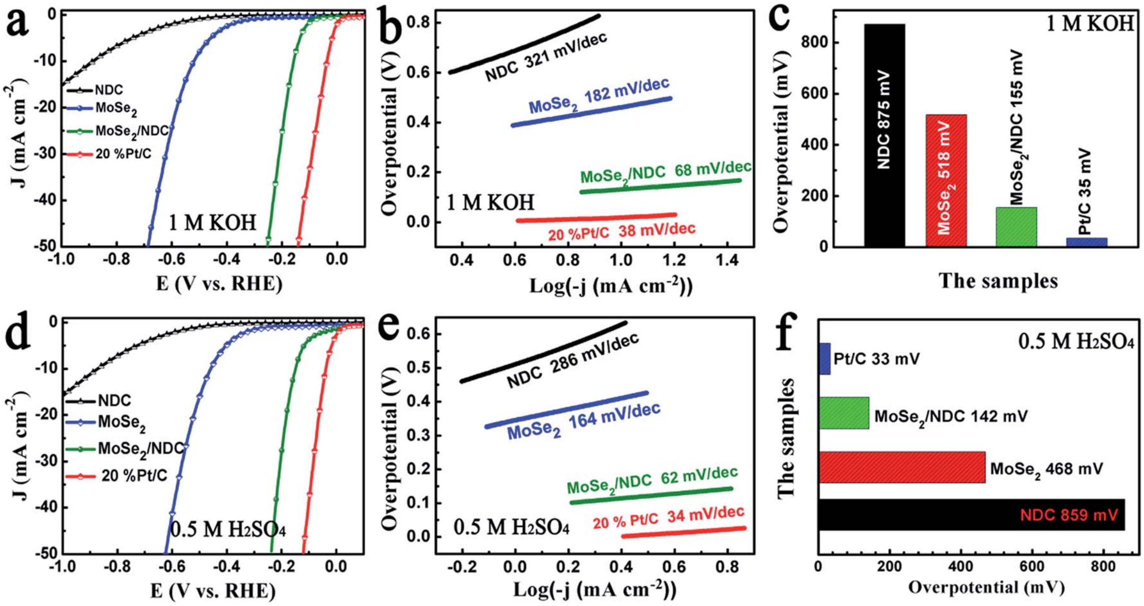

Fig. 3 LSV curves of the NDC, $MoSe_2$, $MoSe_2$/NDC, and 20% Pt/C measured at 5 mV s^{-1} in (a) 1.0 M KOH, and (d) 0.5 M H_2SO_4 for the HER; corresponding Tafel plots in (b) 1.0 M KOH, and (e) 0.5 M H_2SO_4; corresponding overpotential in (c) 1.0 M KOH and (f) 0.5 M H_2SO_4.

HER performances for the NDC, $MoSe_2$, $MoSe_2$/NDC, and 20% Pt/C in acidic media were also tested based on 0.5 M H_2SO_4 electrolyte to demonstrate the pH-universal activity for the HER. As can be seen from Fig. 3d and e, the as-fabricated $MoSe_2$/NDC composites also show a smaller overpotential (142 mV *vs.* RHE) than the pure NDC (859 mV *vs.* RHE) and $MoSe_2$ (468 mV *vs.* RHE) at a current density of 10 mA cm^{-2}, approaching the value of commercial 20% Pt/C (33 mV *vs.* RHE), which indicates the equally higher HER activity of $MoSe_2$/NDC composites in acidic media. In addition, as shown in Fig. 3f, the corresponding Tafel slope values for the pure NDC, $MoSe_2$, $MoSe_2$/NDC and 20% Pt/C were calculated to be 286, 164, 62, and 34 mV dec^{-1}, respectively. Apparently, $MoSe_2$/NDC composites also exhibit a Tafel slope lower than that of pure NDC and $MoSe_2$, and close to that of commercial 20% Pt/C catalyst, proving an equally high HER rate and favorable kinetics of the $MoSe_2$/NDC in acidic media.

According to the mechanism of hydrogen evolution, the HER process can be defined by three principal steps in acidic electrolyte. The Volmer reaction ($H_3O^+ + e^- \rightarrow H_{ads} + H_2O$) occurs in the initial discharge step, which usually possesses a high Tafel slope of 120 mV dec^{-1}. Then, the Heyrovsky reaction (the electrochemical desorption step): $H_{ads} + H_3O^+ + e^- \rightarrow H_2 + H_2O$ and the Tafel reaction (the recombination step): $H_{ads} + H_{ads} \rightarrow H_2$ may appear in the HER process. Consequently, the value of Tafel slopes will significantly be reduced to 40 and 30 mV dec^{-1}.[31,34] By contrast, the Tafel slope of $MoSe_2$/NDC is close to 40 mV dec^{-1}, revealing that the HER may proceed *via* a Volmer–Heyrovsky mechanism.

To further grasp the differences in electrocatalytic performance in alkaline and acidic media, the effective electrochemical active surface areas (ECSAs) of the NDC, $MoSe_2$, and $MoSe_2$/NDC were compared with each other in electrochemical double-layer capacitance (EDLC) values calculated from the CV curve.[32,36] As shown in Fig. 4a and d, both the CV curves of the as-obtained $MoSe_2$/NDC electrocatalysts in 1.0 M KOH and 0.5 M H_2SO_4 exhibit good rectangular consistency, implying facile electron and ion transport in the electrochemical reaction and demonstrating the good conductivity of the catalysts.[37] As further shown in Fig. 4b, the $MoSe_2$/NDC composites have a larger EDLC value (16.5 mF cm^{-2}) compared to NDC (1.5 mF cm^{-2}) and $MoSe_2$ (3.8 mF cm^{-2}) in 1.0 M KOH. Meanwhile, the $MoSe_2$/NDC has a larger EDLC value (19.7 mF cm^{-2} calculated from the CV results as shown in Fig. 4d) than the NDC (1.8 mF cm^{-2}) and $MoSe_2$ (4.9 mF cm^{-2}) in 0.5 M H_2SO_4, as shown in Fig. 4e. In other words, the $MoSe_2$/NDC electrocatalyst have the largest electrochemical active surface area compared to that of the NDC and $MoSe_2$ electrocatalysts, also indicating a superior HER activity of $MoSe_2$/NDC. In addition, the electrochemical active surface area of the $MoSe_2$/NDC catalyst in acidic electrolyte is larger than that in alkaline electrolyte, which can explain the differences in the HER activity of the $MoSe_2$/NDC in alkaline and acidic media.

In order to further shed light on the excellent HER activity of the fabricated $MoSe_2$/NDC in alkaline and acidic media with the demonstrated method, electrochemical impedance spectroscopy (EIS) analyses were further carried out to study the interfacial reactions and electrode kinetics in the HER process. As shown in Fig. 4g, the corresponding Nyquist plots show that the $MoSe_2$/NDC electrocatalyst in alkaline and acidic media exhibits a smaller charge transfer resistance (R_{ct}, the diameter of the semi-circle in the high frequency region, corresponding to the whole resistance between the interfaces of the electrode and electrolyte) of 22.4/18.8 Ω than that of $MoSe_2$ (57.6/54.2 Ω), indicating a faster Faradaic process and better HER kinetics compared to pure $MoSe_2$. This directly confirms the effectiveness of the space-confined growth strategy that involves encapsulating the *in situ* generated $MoSe_2$ sheets with an N-

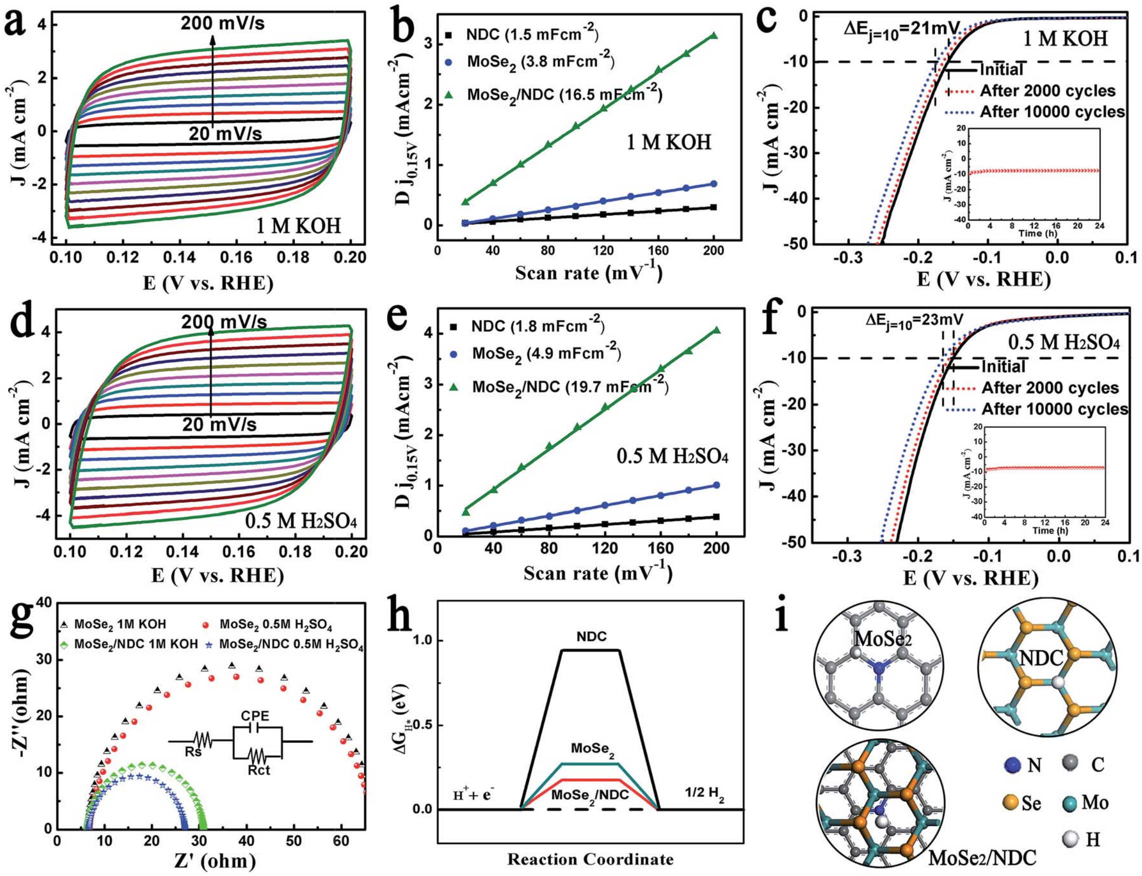

Fig. 4 (a and d) CVs of MoSe$_2$/NDC composites at different scan rates from 20 to 200 mV s^{-1} in 1.0 M KOH/0.5 M H_2SO_4; (b and e) the corresponding estimation of the EDLC value by plotting the current density variation (of $-j_a - j_c$)/2 at 150 mV *versus* RHE; (c and f) durability test for the MoSe$_2$/NDC electrocatalyst before and after 10 000 cycles in 1.0 M KOH/0.5 M H_2SO_4; inset: the time-dependent current density curve of MoSe$_2$/NDC at a static overpotential; (g) Nyquist plots of MoSe$_2$ and MoSe$_2$/NDC composites; (h) the calculated free-energy diagram of the HER at equilibrium for NDC, MoSe$_2$ and MoSe$_2$/NDC; (i) the schematic model of NDC, MoSe$_2$ and MoSe$_2$/NDC with H* adsorbed on its surface.

doped carbon shell to form a hierarchical porous composite structure, which can greatly improve the poor intrinsic conductivity of pure MoSe$_2$ by taking advantage of the excellent electric conductivity of carbonaceous materials and simultaneously facilitate the adsorption of electrolyte, boosting exposure of more active sites for hydrogen atom adsorption, finally resulting in enhanced HER activity. As is known, stability is another key performance metric to assess the catalytic practicability. To investigate the stability of the MoSe$_2$/NDC electrocatalyst in the HER process, the durability of MoSe$_2$/NDC was evaluated through continuous CV cycling between 0.1 and 0.2 V (*vs.* RHE) at a scan rate of 300 mV s^{-1} in 1.0 M KOH/0.5 M H_2SO_4. After 10 000 cycles, the observed overpotential in 1.0 M KOH/0.5 M H_2SO_4 only shows a small decline of 21 mV/23 mV, respectively (Fig. 4c and f). In addition, there is almost no attenuation observed in the time-dependent current density curve of MoSe$_2$/NDC composites at an applied constant overpotential of 155 mV/142 mV up to 24 hours in 1.0 M KOH/0.5 M H_2SO_4 (inset of Fig. 4c and f). Both of the results forcefully demonstrate the excellent stability of MoSe$_2$/NDC during the HER process in alkaline and acidic media, stemming from the protection of an N-doped carbon shell, which can effectively protect the encapsulated MoSe$_2$ nanosheets from corrosion in corrosive electrolyte and maintain the original microstructure after a long cycle of operation as shown in Fig. S3.†

Density functional theory (DFT) calculations

For further insights into the mechanism of the enhanced HER activity of the MoSe$_2$/NDC, density functional theory (DFT) calculations were carried out to calculate the Gibbs free energy of H* absorption (ΔG_{H^*}), which was regarded as a descriptor of the HER activity of the catalyst.[50] A good HER catalyst should have a nearly zero $|\Delta G_{H^*}|$.[6,51] In this work, the ΔG_{H^*} of NDC, pure MoSe$_2$, and MoSe$_2$/NDC was calculated as shown in Fig. 4h. The corresponding theoretical models are shown in Fig. 4i, respectively. The active adsorption site for H* was on the edge Se atom in pure MoSe$_2$ and MoSe$_2$/NDC, and the H* was adsorbed on the C atom coordinated with the doped N atom in N-doped carbon, which are consistent with previous work.[43,52] The calculated results show that the ΔG_{H^*} of NDC is very large, indicating that its adsorption ability for H* is unsatisfactory. MoSe$_2$/NDC has a reduced ΔG_{H^*} (0.16 eV) compared with MoSe$_2$, which demonstrates that the existence of NDC led to accelerated adsorption and desorption steps of H* on MoSe$_2$.

Table 1 List of the HER catalytic metrics of the $MoSe_2$/NDC composites and previously reported $MoSe_2$-based catalysts in alkaline and acidic media

Catalysts	Electrolyte	E_{onset}/mV (*vs.* RHE)	$E\eta_{10}$/mV (*vs.* RHE)	Tafel slope (mV dec^{-1})	Ref.
$MoSe_2$/NDC	1.0 M KOH	**−83**	**−155**	**68**	This work
Co_4Mo_0@NC	1.0 M KOH	−140	−218	73.5	13
$CoSe_2$–$MoSe_2$/rGO–C	1.0 M KOH	−125	−215	83.2	44
$MoSe_2$–$CoSe_2$ CNTs	1.0 M KOH	−127	−237	89	49
$MoSe_2$/NDC	0.5 M H_2SO_4	**−58**	**−142**	**62**	This work
$MoSe_2$-E	0.5 M H_2SO_4	−120	−180	71	28
MoO_2/$MoSe_2$	0.5 M H_2SO_4	−101	−167	68	30
$MoSe_2$ HDH	0.5 M H_2SO_4	−110	−191	72	34
$MoSe_2$ nanostructures	0.5 M H_2SO_4	−130	−228	92	37
HD-p$MoSe_2$/NG	0.5 M H_2SO_4	NA	−106	57	40
$MoSe_2$–rGO–CNT	0.5 M H_2SO_4	NA	−240	53	42

The theoretical simulations agree well with the experimental results that $MoSe_2$/NDC has a significantly reduced overpotential compared with pure $MoSe_2$. Based on the above analysis, it can be deduced that the space-confined growth of $MoSe_2$ sheets in an N-doped carbon shell can synergistically enhance the overall HER activity.

In order to intuitively demonstrate the excellent HER performance of the as-fabricated $MoSe_2$/NDC composite electrocatalysts, their HER catalytic metrics were compared with those of currently reported state-of-the-art $MoSe_2$-based electrocatalysts in alkaline/acidic media. As summarized in Table 1, whether in acidic or alkaline media, the electrocatalytic activities of the as-synthesized $MoSe_2$/NDC composites are superior to those of the previously reported state-of-the-art $MoSe_2$-based catalysts in terms of the lowest onset potential, overpotential and Tafel slope value. We suggest that the excellent HER performance of the $MoSe_2$/NDC composites fabricated with our strategy can be attributed to the following reasons: first, the space-confined growth of $MoSe_2$ nanosheets in an N-doped carbon shell can effectively inhibit their aggregation in the process of synthesis, providing more active sites accessible to the electrolyte for hydrogen atom adsorption and the HER. Second, the N-doped carbon shell not only can serve as a carrier with high electric conductivity to improve the intrinsic poor conductivity of $MoSe_2$ nanosheets, promoting the electron transport and charge transfer at the interface, but also serve as a protection layer to prevent encapsulated $MoSe_2$ nanosheets from corrosion, resulting in enhanced durability during the HER process both in alkaline and acidic media. Finally, the synchronous construction of a flower-like hierarchical porous structure facilitates the adsorption of electrolyte, boosting exposure of more active sites for hydrogen atom adsorption.

Conclusion

In summary, space-confined $MoSe_2$ nanosheets grown in an N-doped carbon shell with a hierarchical porous structure ($MoSe_2$/NDC) were designed and fabricated with a simple strategy. Benefiting from the rational structure design, the as-fabricated $MoSe_2$/NDC composites acquire improved conductivity and more exposed active sites for hydrogen atom adsorption, and exhibit excellent HER activity both in alkaline and acidic media with a small overpotential of 155 mV/142 mV at a current density of 10 mA cm^{-2}, and a Tafel slope of 68 mV dec^{-1}/62 mV dec^{-1}, respectively, superior to those of the currently reported state-of-the-art $MoSe_2$-based catalysts, and close to that of 20 wt% Pt/C. More importantly, thanks to the protection of the outermost N-doped carbon layer, the $MoSe_2$/NDC composites show excellent durability with almost no attenuation observed in the time-dependent current density curve at an applied constant overpotential of 155 mV/142 mV up to 24 hours in alkaline/acidic media. Theoretical calculations further verified that the presence of the NDC optimized adsorption and desorption behavior of H* on $MoSe_2$, which proves the advanced HER catalytic activity of $MoSe_2$/NDC. This work paved a new way for synthesizing highly efficient $MoSe_2$-based pH-universal electrocatalysts toward hydrogen production.

Conflicts of interest

There are no conflicts to declare.

Acknowledgements

This work was financed by the National Natural Science Foundation of China (51871001 and 51672001), Open fund for Discipline Construction, Institute of Physical Science and Information Technology, Anhui University (S01003102), National Key R&D Program of China (2017YFA0403600), Outstanding Youth Fund of Anhui Province (1808085J10), International cooperation fund of Anhui Province (1704e1002209), and the open project of Anhui Province Key Laboratory of Advanced Catalytic Materials and Reaction Engineering.

Notes and references

1 M. S. Faber and S. Jin, *Energy Environ. Sci.*, 2014, **7**, 3519–3542.
2 Z. W. Seh, J. Kibsgaard, C. F. Dickens, I. Chorkendorff, J. K. Nørskov and T. F. Jaramillo, *Science*, 2017, **355**, 1–12.

3 J. Luo, J. H. Im, M. T. Mayer, M. Schreier, M. K. Nazeeruddin, N. G. Park and M. Grätzel, *Science*, 2014, **345**, 1593–1597.
4 W. Zhou, J. Zhou, Y. Zhou, J. Lu, K. Zhou, L. Yang, Z. Tang, L. Li and S. Chen, *Chem. Mater.*, 2015, **27**, 2026–2032.
5 P. Jiang, J. Chen, C. Wang, K. Yang, S. Gong, S. Liu, Z. Lin, M. Li, G. Xia, Y. Yang, J. Su and Q. Chen, *Adv. Mater.*, 2018, **30**, 1705324.
6 Y. Wen, Y. Xia and S. Zhang, *J. Power Sources*, 2016, **307**, 593–598.
7 L. Zhang, J. S. Hu, X. H. Huang, J. Song and S. Y. Lu, *Nano Energy*, 2018, **48**, 489–499.
8 A. J. Bard and M. A. Fox, *Acc. Chem. Res.*, 1995, **28**, 141–145.
9 M. Dresselhaus and I. Thomas, *Nature*, 2001, **414**, 332–337.
10 M. G. Walter, E. L. Warren, J. R. McKone, S. W. Boettcher, Q. Mi, E. A. Santori and N. S. Lewis, *Chem. Rev.*, 2010, **110**, 6446–6473.
11 J. R. McKone, E. L. Warren, M. J. Bierman, S. W. Boettcher, B. S. Brunschwig, N. S. Lewis and H. B. Gray, *Energy Environ. Sci.*, 2011, **4**, 3573–3583.
12 X. Xiao, L. Tao, M. Li, X. Lv, D. Huang, H. Pan, M. Wang and Y. Shen, *Chem. Sci.*, 2018, **9**, 1970–1975.
13 J. Jiang, Q. Liu, C. Zeng and L. Ai, *J. Mater. Chem. A*, 2017, **5**, 16929–16935.
14 L. Ai, T. Tian and J. Jiang, *ACS Sustainable Chem. Eng.*, 2017, **5**, 4771–4777.
15 X. Wang, H. Zhou, D. Zhang, M. Pi, J. Feng and S. Chen, *J. Power Sources*, 2018, **387**, 1–8.
16 W. Chen, J. Pei, C. T. He, S. Lu, L. Zheng, X. Zheng, W. Yan, Z. Zhuang, C. Chen, Q. Peng, D. Wang and Y. D. Li, *Angew. Chem., Int. Ed.*, 2017, **56**, 16086–16090.
17 X. Fan, Y. Liu, Z. Peng, Z. Zhang, H. Zhou, X. Zhang, B. I. Yakobson, W. A. Goddard, X. Guo, R. H. Hauge and J. M. Tour, *ACS Nano*, 2017, **11**, 384–394.
18 J. Wan, J. Wu, X. Gao, T. Li, Z. Hu, H. Yu and L. Huang, *Adv. Funct. Mater.*, 2017, **27**, 1703933.
19 S. K. Kim, D. Yoon, S. C. Lee and J. Kim, *ACS Catal.*, 2015, **5**, 3292–3303.
20 Y. C. Liu, B. B. Huang, X. Hu and Z. L. Xie, *Int. J. Hydrogen Energy*, 2019, **44**, 3702–3710.
21 Y. C. Liu, B. B. Huang and Z. L. Xie, *Appl. Surf. Sci.*, 2018, **427**, 693–701.
22 H. Yan, Y. Xie, Y. Jiao, A. Wu, C. Tian, X. Zhang, L. Wang and H. Fu, *Adv. Mater.*, 2018, **30**, 1704156.
23 X. Zhang, X. Yu, L. Zhang, F. Zhou, Y. Liang and R. Wang, *Adv. Funct. Mater.*, 2018, **28**, 1706523.
24 Z. X. Wu, J. Wang, K. D. Xia and W. Lei, *J. Mater. Chem. A*, 2017, **6**, 616–622.
25 Q. Xiong, X. Zhang, H. Wang, G. Liu, G. Wang, H. Zhang and H. Zhao, *Chem. Commun.*, 2018, **54**, 3859–3862.
26 M. Cai, F. Zhang, C. Zhang, C. Lu, Y. He, Y. Qu, H. Tian, X. Feng and X. Zhuang, *J. Mater. Chem. A*, 2018, **6**, 138–144.
27 S. Su, Q. Zhou, Z. Zeng, D. Hu, X. Wang, M. Jin, X. Gao, R. Nötzel, G. Zhou, Z. Zhang and J. Liu, *ACS Appl. Mater. Interfaces*, 2018, **10**, 8026–8035.
28 Q. Jiang, Y. Lu, Z. Huang and J. Hu, *Appl. Surf. Sci.*, 2017, **402**, 277–285.
29 Y. Yin, Y. Zhang, T. Gao, T. Yao, X. Zhang, J. Han, X. Wang, Z. Zhang, P. Xu, P. Zhang, X. Cao, B. Song and S. Jin, *Adv. Mater.*, 2017, **29**, 1700311.
30 J. Luo, P. Xu, D. Zhang, L. Wei and D. Zhou, *Nanotechnology*, 2017, **28**, 465404.
31 C. Jian, Q. Cai, W. Hong, J. Li and W. Liu, *Small*, 2018, **14**, 1703798.
32 H. Peng, C. Wei, K. Wang, T. Meng, G. Ma, Z. Lei and X. Gong, *ACS Appl. Mater. Interfaces*, 2017, **9**, 17067–17075.
33 L. Zhang, T. Wang, L. Sun, Y. Sun, T. Hu, K. Xu and F. Ma, *J. Mater. Chem. A*, 2017, **5**, 19752–19759.
34 B. Mao, T. Bao, J. Yu, L. Zheng, J. Qin, W. Yin and M. Cao, *Nano Res.*, 2017, **10**, 2667–2682.
35 H. Shu, D. Zhou, F. Li, D. Cao and X. Chen, *ACS Appl. Mater. Interfaces*, 2017, **9**, 42688–42698.
36 D. Gao, B. Xia, Y. Wang, W. Xiao, P. Xi, D. Xue and J. Ding, *Small*, 2018, **14**, 1704150.
37 W. Guo, Y. Chen, L. Wang, J. Xu, D. Zeng and D. L. Peng, *Electrochim. Acta*, 2017, **231**, 69–76.
38 S. Deng, Y. Zhong, Y. Zeng, Y. Wang, Z. Yao, F. Yang, S. Lin, X. Wang, X. Lu, X. Xia and J. Tu, *Adv. Mater.*, 2017, **29**, 1700748.
39 W. D. Li, Y. Liu, M. Wu, X. L. Feng, K. F. Wu, Z. Y. Liu, B. J. Li, Z. M. Chen and S. Y. Lu, *Adv. Mater.*, 2018, **30**, 1800676.
40 M. Zhuang, Y. Ding, X. Ou and Z. Luo, *Nanoscale*, 2017, **9**, 4652–4659.
41 Y. Han, Y. G. Wang, W. Chen, R. Xu, Y. Zhu, W. C. Cheong, C. Chen, Q. Peng, D. Wang and Y. D. Li, *J. Am. Chem. Soc.*, 2017, **139**, 17269–17272.
42 G. D. Park, J. H. Kim, S. K. Park and Y. C. Kang, *ACS Appl. Mater. Interfaces*, 2017, **9**, 10673–10683.
43 F. Lai, D. Yong, X. Ning, B. Pan, Y. E. Miao and T. Liu, *Small*, 2017, **13**, 1602866.
44 B. Wang, Z. G. Wang, X. Q. Wang, B. J. Zheng, W. L. Zhang and Y. F. Chen, *J. Mater. Chem. A*, 2018, **6**, 12701–12707.
45 T. J. Dai, X. D. Fan, Y. X. Ren, S. Hou, Y. Y. Zhang, L. X. Qian, Y. R. Li and X. Z. Liu, *J. Mater. Sci.*, 2018, **53**, 8436–8444.
46 N. Xue and P. Diao, *J. Phys. Chem. C*, 2017, **121**, 26686–26697.
47 Z. Q. Cao, M. Z. Wu, H. B. Hu, G. J. Liang and Z. Y. Zhi, *NPG Asia Mater.*, 2018, **10**, 670–684.
48 D. Damien, A. Anil, D. Chatterjee and M. M. Shaijumon, *J. Mater. Chem. A*, 2017, **5**, 13364–13372.
49 X. Q. Wang, B. J. Zheng, B. Wang, W. L. Zhang and Y. F. Chen, *J. Mater. Chem. A*, 2018, **6**, 7842–7850.
50 L. Zhang, Y. T. Chen, P. P. Zhao, W. Luo, S. L. Chen and M. H. Shao, *Electrocatalysis*, 2018, **9**, 264–270.
51 W. X. Chen, J. J. Pei, C. T. He, Z. B. Zhuang, Q. Peng, D. S. Wang and Y. D. Li, *Adv. Mater.*, 2018, **30**, 1800396.
52 S. Liu, M. S. Li, C. L. Wang, P. Jiang, L. Hu and Q. W. Chen, *ACS Sustainable Chem. Eng.*, 2018, **6**, 9137–9144.